Contributions to Mineralogy and Petrology (2022) 177:66
https://doi.org/10.1007/s00410-022-01929-2

ORIGINAL PAPER

Arsenopyrite oxidative dissolution in NaCl solution at high-temperature and high-pressure conditions: kinetics, pathways, dissolution mechanism and geological implications

Qingyou Liu[1] · Kai Zheng[1,2] · Shuai Wang[1,3] · Luying Wang[1] · Sen Lin[1] · Heping Li[1]

Received: 14 February 2022 / Accepted: 3 June 2022 / Published online: 23 June 2022

Abstract

Arsenopyrite (FeAsS) is one of the sulfide minerals of seafloor massive sulfide deposits. The presence of sodium chloride and high-temperature and high-pressure (HTHP) geological conditions seriously affect the process of arsenopyrite weathering. However, electrochemical oxidative dissolution has never been considered in the context of seafloors, though it has already been shown to increase dissolution significantly in terrestrial deposits. In this work, in situ electrochemical techniques and surface analysis were used to investigate the behaviors of oxidative arsenopyrite dissolution in different concentrations of NaCl at temperatures ranging from 280 to 360 °C and pressures ranging from 12.0 to 20.0 MPa. In the initial stage, arsenopyrite was oxidized to S^0, As(III), and Fe(II). The S^0 and As(III) were ultimately converted into SO_4^{2-} and AsO_4^{3-} and entered the solution. The Fe(II) was converted into α-FeOOH, γ-FeOOH, and Fe_2O_3 as a passivation film. The presence of Cl^- ions promoted the oxidative dissolution of arsenopyrite without changing its oxidation mechanism. Higher temperatures or greater pressures promoted the oxidative dissolution of arsenopyrite by enhancing charge migration and ion diffusion. Under the experimental HTHP conditions, the oxidative arsenopyrite dissolution rate constant was 8.0×10^{-5} mol•m^{-2}•s^{-1}. This work expands the understanding of the geochemical cycles of Fe, As and S and provides an experimental basis for the formation of secondary minerals from arsenopyrite weathering under the hydrothermal solution conditions of the seafloor.

Keywords Arsenopyrite · NaCl · Electrochemical oxidation · High temperature and high pressure · Geological implications

Communicated by Gordon Moore.

✉ Heping Li
liheping@vip.gyig.ac.cn

Qingyou Liu
liuqingyou@mail.gyig.ac.cn

Kai Zheng
zhengkai@gnnu.edu.cn

Shuai Wang
wangshuai@mail.gyig.ac.cn

Luying Wang
wangluying@mail.gyig.ac.cn

Sen Lin
linsen@mail.gyig.ac.cn

[1] Key Laboratory of High-Temperature and High-Pressure Study of the Earth's Interior, Institute of Geochemistry, Chinese Academy of Sciences, Guiyang 550081, China

[2] Gannan Normal University, Ganzhou 341400, China

[3] University of Chinese Academy of Sciences, Beijing 100049, China

Introduction

Arsenopyrite is an abundant arsenic-bearing mineral found on and below the Earth's surface. Its solubility in hydrothermal fluids affects the geochemical cycles of arsenic, sulfur and iron and acts as an important constraint on the circulation of other related elements at the surface, on the sea floor, and within the Earth's interior. From the viewpoint of thermodynamics, arsenopyrite easily oxidizes and decomposes in acidic and basic media (Osseo-Asare et al. 1984; Papangelakis and Demopoulos 1990a). In contrast, from the viewpoint of kinetics, arsenopyrite is an inert mineral resistant to oxidization (Papangelakis and Demopoulos 1990b). Many studies have shown that the oxidative dissolution of arsenopyrite is affected not only by its own properties and structure but also by different environmental factors. Oxidizing agents such as oxygen (Wang et al. 2018; Walker et al. 2006), high-valence metal ions (Neil and Jun 2016), and high-valence acid atomic groups (Lin et al. 2018) tend to gain electrons during the oxidization of arsenopyrite, thus

promoting its dissolution. The pH of the solution is one of the most important parameters controlling the oxidation of arsenopyrite because H^+ and OH^- participate in such reactions. Generally, acidic conditions promote arsenopyrite oxidation, while neutral and basic conditions inhibit arsenopyrite oxidation by forming Fe oxides on the arsenopyrite surface (Yu et al. 2004b, 2007; McKibben et al. 2008). Temperature changes the charge transfer rate of oxidizing ions (Fe^{3+} ions) and thus seriously affects the oxidation rate of arsenopyrite (Yu et al. 2004a) and the product speciation. Fernandez et al. (1996b) pointed out that the product speciation of arsenopyrite in a pH 2 chloride solution was dependent on temperature and potential but not on the arsenopyrite composition.

Arsenopyrite is a diamagnetic semiconductor owing to its electronic structure (or chemical bonding) (Pearce et al. 2006; Li et al. 2015). In the presence of electrolytes, the oxidative dissolution of arsenopyrite is considered an electrochemical process in nature. Regarding arsenopyrite oxidation in acidic conditions, Richardson and Vaughan (1989) confirmed the enrichment of iron and arsenic on the surface in an H_2SO_4 solution. However, several researchers (Buckley and Walker 1988; Nesbitt and Muir 1998; Mikhlin et al. 2006) observed the depletion of Fe and As from the passivation film and the absence of S from the surface. Under acidic conditions, a metal-deficient sulfide layer is generally observed at the initial stage of arsenopyrite oxidation, and the results showed that stoichiometric, sulfur-deficient and arsenic-deficient arsenopyrite have practically the same oxidation rate (Fernandez et al. 1996a). Lazaro et al. (1997) and Li et al. (2006) revealed that arsenopyrite first decomposes to As_2S_2, which covers the electrode and delays the dissolution of arsenopyrite. Subsequently, As_2S_2 is oxidized to H_3AsO_3, H_3AsO_3 is oxidized to H_3AsO_4, and Fe^{2+} is oxidized to Fe^{3+} with increasing potential. With the development of synchrotron radiation technology, Mikhlin and Tomashevich (2005) demonstrated the oxidization of arsenopyrite to an As- (As^{3+}, As^{5+}, and As^{1-}) and Fe-rich (Fe(II)–(As–S), Fe(III)–(As–S)) integument with a subjacent S-enriched layer (S_2^{2-}, S^{2-} and S_2^{2-}), and their results were consistent with the report by Nesbitt et al. (1995). Arsenopyrite oxidation in basic solution at room temperature and atmospheric pressure is generally recognized as a two-step reaction. However, a consensus on the products of the initial step has not been reached. Sanchez and Hiskey (1991) investigated the electrochemical oxidation of arsenopyrite within a pH range from 8.0 to 12.0 in the absence and presence of cyanide (0.01 M). They observed the initial step products of $Fe(OH)_3$, $H_2AsO_3^-$ and S°, which were converted into $HAsO_4^-$ and SO_4^{2-} in the second step. At pH values of 8.1–12.0 and cyanide concentrations from 10^{-4} to 10^{-2} M, Sanchez and Hiskey (1998) revealed the initial formation of FeOOH, SO_4^{2-} and $H_2AsO_3^-$, after which $H_2AsO_3^-$ was further oxidized to $HAsO_4^-$. Nicol and Guresin (2003) reported that in the presence of ferrate (VI) and oxygen in basic solution, the oxidation of arsenopyrite first produced $Fe(OH)_3$, AsO_3^{3-} and SO_4^{2-}, and then the AsO_3^{3-} transformed into AsO_4^{3-}.

Chlorine is one of the most abundant elements on Earth and is widely found on the surface and in the interior. The presence of chloride ions affects arsenopyrite oxidation via the formation of iron(II) chloride complexes (Heinrich and Seward 1990) and iron(III) chloride complexes (Stefánsson et al. 2019). Moreover, chloride ions have a strong penetrating ability and can penetrate the surface film, thus promoting the dissolution of arsenopyrite (Zheng et al. 2020a). Neil et al. (2014) studied arsenic mobilization from arsenopyrite oxidation at managed aquifer recharge sites in the presence of NaCl. The results revealed that arsenopyrite was oxidized to iron(III) (hydr)oxide precipitates and caused α-Fe_2O_3 formation, which decreased the available surface area for arsenic attenuation. In geological areas, chloride ions affect the formation of secondary minerals, the enrichment of precious metals and the formation of arsenopyrite inclusions. Mikhlin et al. (2006) studied the surfaces of natural auriferous arsenopyrite samples and confirmed that chloride ions affect gold deposition. Groznova et al. (2006) investigated the mineralogy and pressure–temperature formation conditions of the Dzhimidon Pb–Zn deposit in the Sadon ore district and confirmed the important effects of chloride ions on sulfide deposits.

Limited by experimental techniques and means, the oxidative dissolution behavior of arsenopyrite under high-pressure hydrothermal conditions, such as deep-sea hydrothermal environments, has rarely been investigated from the perspective of electrochemical reactions. The few existing studies have only focused on the target components of arsenopyrite dissolved in high-temperature pressure vessels after quenching (Pokrovski et al. 2002; Tyukova and Voroshin 2004) or deduced the metallogenic environment of arsenopyrite and its secondary minerals from the inclusions (Parthasarathy et al. 2016). In this work, the oxidative dissolution behavior of arsenopyrite in 0–0.40 mol·L^{-1} sodium chloride solution at high temperature (280–360 °C) and high pressure (12.0–20.0 MPa) was investigated using in situ electrochemical techniques and surface analysis. We aimed to quantitatively obtain the thermodynamic and kinetic parameters of arsenopyrite oxidation and reveal the oxidation mechanism of arsenopyrite under high-temperature and high-pressure (HTHP) conditions. The experimental results will expand the understanding of the geochemical cycles of Fe, As and S and provide the experimental basis for the element release and the formation of secondary minerals from arsenopyrite oxidative dissolution under HTHP conditions.

Experimental

Arsenopyrite specimens and electrode preparation

Arsenopyrite specimens were collected from the Jinya gold deposit in Fengshan of the Guangxi Zhuang Autonomous Region, China. The arsenopyrite specimens were first crushed to 60–80 mesh particles. Subsequently, arsenopyrite particles were artificially selected under a microscope. The scanning electron microscopy (SEM) and backscattered electron results showed the absence of chemical zoning and heterogeneity in the particles. The composition of arsenopyrite (Wt.%) was determined through quantitative EPMA analysis as follows: 33.580% Fe, 46.101% As, and 19.238% S (Table S1). The arsenopyrite particles were ground to 200-mesh in ethanol, dried under vacuum, and compressed into a 6 mm in diameter and 8 mm in length cylinder under 1.0 MPa. Thereafter, the cylinder was wrapped with silver foil for air insulation and then placed inside a boron nitride and pyrophyllite mold. The boron nitride and pyrophyllite acted as the pressure-transmitting medium. A stainless-steel sheet was used for heating, and a K-type thermocouple was used for temperature control. Finally, the cylinder sample was subjected to hot-pressure sintering using a six-axis multi-anvil press. The hot-pressure sintering state was maintained at a temperature of 500 °C and pressure of 1.0 GPa for 2 h, with heating and cooling rates of 10 °C/min and 3 °C/min, respectively. EPMA, XRD, and Raman spectroscopy were used to analyze the obtained arsenopyrite samples, and the tests confirmed that the samples were pure, corresponding to the molecular formula $Fe_{1.00}As_{1.02}S_{1.03}$. Furthermore, a numerically controlled machine tool was used to cut the samples into circular truncated cones to suit the autoclave stopper. The operations of the arsenopyrite hot-pressure sintering equipment according to the manufacturer are detailed by Zheng et al. (2020b).

HTHP interaction and electrochemical measurements

A self-designed autoclave made of titanium alloy was used to investigate the electrochemical oxidation of arsenopyrite under HTHP conditions. A resistance furnace was used as a heater, and the temperature was moderated with a temperature controller (± 0.5 °C) through a thermocouple placed near the experimental arsenopyrite specimen. The pressure of the inner autoclave was sensitized for detection using a pressure sensor, and a pressure pump was installed for adjustments.

A PARSTAT 2273 (Princeton Applied Research) electrochemical workstation and three-electrode configuration were adopted for the electrochemical experiments. The working electrode was a massive hot-pressure-sintered arsenopyrite sample. A homemade platinum electrode was used as the counter electrode; to make this electrode, platinum was sintered onto an alumina ceramic, and the electrons were conducted by a platinum wire through the central axis of the alumina ceramic. The reference electrode was an external pressure balanced Ag/AgCl electrode. The electrolyte was 0.1 M KCl, and Eq. (1) is used to calibrate the electrode potential (Macdonald et al. 1979). During the experiments, pyrophyllite taper sleeves were used to seal and insulate the counter and working electrodes from the autoclave. A schematic diagram of the installation of the hydrothermal reaction device and assembly of the three electrodes is presented in Fig. S1. The device was described in detail by Lin et al. (2017). Prior to the electrochemical tests, 2500-grit silicon carbide abrasive paper was used to obtain a flat, clean surface:

$$E_{\mathrm{SHE}} = E_{\mathrm{obs}} + 0.2866 - 0.001(T - 298.15) + 1.745 \times 10^{-7}(T - 298.15)^2 - 3.03 \times 10^{-9}(T - 298.15)^3 \quad (1)$$

where E_{SHE} is the potential of the saturated hydrogen electrode (SHE), V; E_{obs} is the potential of the experimental observation, V; and T is the absolute temperature of the experiment, K. In this work, all the potentials mentioned were normalized with respect to the SHE using the formula above, unless stated otherwise.

The open-circuit potential (OCP) was measured, and the electrochemical experiments started only when the OCP reached a quasi-steady state, where the quasi-steady is defined as a change of less than 2.0 mV per 5 min. The electrode potential was allowed to stabilize for 20 min before commencement of the measurements. The polarization curve was drawn to determine the weathering dynamics of oxidative arsenopyrite dissolution from -250 to + 250 mV (vs. open current potential, OCP) at a scan rate of 10 $mV \cdot s^{-1}$. Electrochemical impedance spectroscopy (EIS) was conducted to obtain information on the interface and structure of arsenopyrite oxidation at frequencies ranging from 0.001 to 10,000 Hz with an amplitude of 10 mV (vs. OCP).

Surface characterization measurements

The polished arsenopyrite specimens (cuboid with 0.5 cm × 0.5 cm × 0.2 cm) were soaked in solutions of different concentrations of NaCl and maintained for 2 h at the target temperature and pressure. After cooling to room temperature, the specimens were removed for further microscopic examination of morphology changes and analysis of the microstructure of the atomic and molecular functional groups. First, X-ray photoelectron spectroscopy (XPS)

analysis was performed (PHI Quantera SXM) using the Al K α line (energy: 1486.6 eV) as the excitation source, a target voltage of 15 kV, power of 25 W, vacuum degree of 1.33 μPA, data processing and photoelectron peak analysis using multipeak 8.0, peak fitting using the Avantage 5.948 curve fitting program, and the adventitious C 1 *s* contamination peak (284.8 eV) for calibration. Then, SEM (JSM-6460LV) and energy-dispersive spectrometry (EDS) measurements were taken for further surface morphology study and elemental analysis. Finally, Raman spectroscopy (Invia, Renishaw 2000, England) was performed at a wavelength of 514 nm and a collection time of 10 s with a laser power of 50 mW to prevent the destruction of the arsenopyrite samples.

Results

Electrochemical measurements

Open-circuit potential (OCP) study

The open-circuit potential (OCP) reflects the rest potential state of the material. The OCP indicates the tendency to corrode; this is a conductive material with a stronger negative potential that always tends towards corrosion. Generally, factors affecting the OCP include the electrolyte composition and concentration, temperature, and pressure. In the actual geological environment, these factors are reflected by the composition and salinity of the solution surrounding the mineral, environmental temperature, and pore pressure of the mineral. The OCPs of arsenopyrite in sodium chloride solution at different concentrations, temperatures, and pressures are shown in Fig. 1 and Table 1.

In solutions with different concentrations of NaCl at 320 °C and 12.0 MPa, the OCP of arsenopyrite first increased and then reached a quasi-steady state at approximately 40 min, indicating the spontaneous formation of a passive film, as shown in reaction (2) (Deng and Gu 2018). The steady-state OCPs were approximately − 17.3, − 178.1, − 210.2, and − 239.5 mV, respectively. The results revealed that the presence of NaCl strongly affected the OCP of arsenopyrite, and a higher NaCl concentration caused the OCP to be more negative because the chloride ions released by the ionization of NaCl through reaction (3) underwent complexation with ferrous ions to form iron chloride compounds (reaction (4)). The formation of chloride complexes exhausted the supply of iron ions in the solution, disturbing the balance of minerals and metal ions. To become balanced again, the mineral required strong oxidation to produce more ferrous ions, further shifting the OCP towards more negative values:

$$\mathrm{FeAsS(s)} + 3\mathrm{H_2O(l)} \rightarrow \mathrm{AsO_3^{3-}(aq)} + \mathrm{Fe^{2+}(aq)} + \mathrm{S^0(s)} + 6\mathrm{H^+(aq)} + 5\mathrm{e^-} \quad (2)$$

$$\mathrm{NaCl(s)} \leftrightarrow \mathrm{Na^+(aq)} + \mathrm{Cl^-(aq)} \quad (3)$$

$$\mathrm{Fe^{2+}(aq)} + 2\mathrm{Cl^-(aq)} \rightarrow \mathrm{FeCl_2(s)} \quad (4)$$

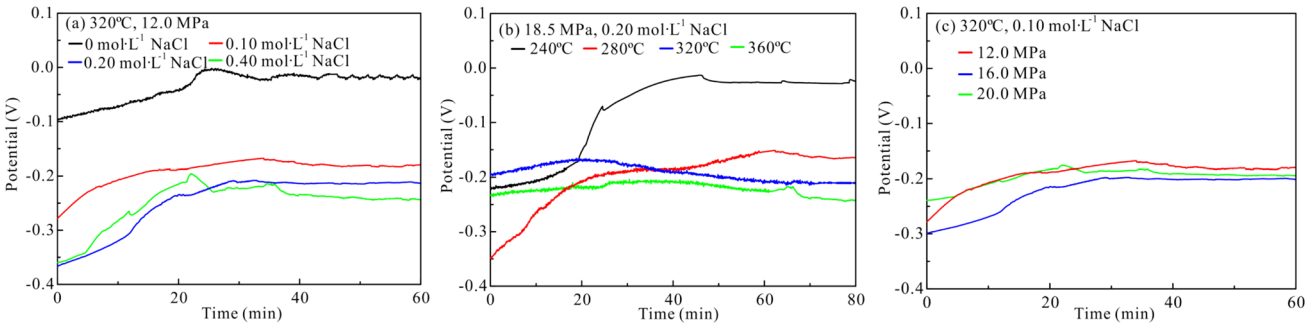

Fig. 1 Time-potential relationships of arsenopyrite electrode, where **a** different concentrations NaCl solution, **b** different temperatures and **c** different pressures

Table 1 Open-circuit potential of arsenopyrite at different conditions

	Different concentrations (mol·L^{-1}) (320 °C, 12.0 MPa)				Different temperatures (°C) (0.20 mol·L^{-1}, 18.5 MPa)				Different pressures (MPa) (320 °C, 0.10 mol·L^{-1})		
	0	0.10	0.20	0.40	240	280	320	360	12.0	16.0	20.0
OCP (mV)	− 17.3	− 178.1	− 210.2	− 239.5	− 26.9	− 162.0	− 210.2	− 244.7	− 178.4	− 192.7	− 199.9

When arsenopyrite was oxidized in NaCl solution under different temperatures or different pressures, both OCP values tended towards negative values with increasing temperature or pressure. These results revealed that arsenopyrite easily corroded under HTHP conditions.

Polarization curves study

The polarization curve is an effective means of studying the oxidative behavior of arsenopyrite from the perspectives of kinetics and thermodynamics. The polarization curves of arsenopyrite in NaCl solution at HTHP are shown in Fig. 2a–c.

When the electrolytes contained different concentrations of NaCl at 320 °C and 12.0 MPa, the arsenopyrite polarization curves exhibited similar polarization profiles (Fig. 2a), suggesting that they had the same oxidative mechanism. In the presence of NaCl, the polarization curve shifted dramatically along the positive of the X-axis and the negative of the Y-axis, and the same shift continued with increasing concentrations of NaCl. All these phenomena suggest that the increase in NaCl concentration increased the corrosion current density (i_{corr}) and shifted the corrosion potential (E_{corr}) towards more negative values. The quantitative electrochemical parameters E_{corr} and i_{corr} were calculated according to the Tafel extrapolation (Bard and Faulkner 2001) and are listed in Table 2. The results showed a larger i_{corr} value with higher NaCl concentrations, suggesting that NaCl promotes the oxidative dissolution of arsenopyrite because higher concentrations of NaCl led to more severe destruction of the passivation film, resulting in the significant oxidization of arsenopyrite.

Figure 2b and c presents the polarization curves of arsenopyrite oxidation at different temperatures and pressures, respectively. The results revealed similar polarization profiles, indicating similar electrochemical interaction mechanisms. Furthermore, higher temperatures or greater pressures caused the polarization curves to shift to the positive side of the X-axis and the negative side of the Y-axis, meaning that i_{corr} increased and E_{corr} shifted towards negative values. The reasons for this behavior are as follows: high temperatures accelerate the transfer of charge through electric double layer, while high pressures compress the thickness of electric double layer and decrease the distance from mineral surface to the outer Helmholtz plane. The detailed explain will be further elucidation at the following EIS study.

EIS study

EIS is used to investigate the fundamental processes of diffusion and Faradaic reactions at electrodes (Lasia 2002). Figure 3 shows the Nyquist and Bode plots for arsenopyrite in solutions with different concentrations of NaCl at 320 °C and 12.0 MPa. The Bode curves revealed three time constants, and the Nyquist curves further confirmed two capacitive loops and a diffusion tail. The loop at high frequencies originated from the pseudo-capacitance impedance for passive behavior and the passivation resistance R_f. The loop at

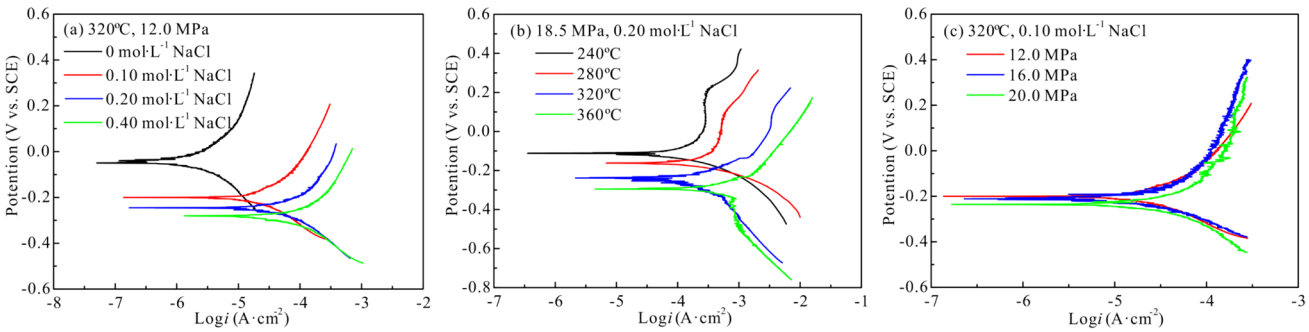

Fig. 2 Polarization curve of arsenopyrite electrode, where **a** different concentrations NaCl solution, **b** different temperatures and **c** different pressures

Table 2 Tafel parameter of arsenopyrite

	Different concentrations (mol·L^{-1}) (320 °C, 12.0 MPa)				Different temperatures (°C) (0.20 mol·L^{-1}, 18.5 MPa)				Different pressures (MPa) (320 °C, 0.10 mol·L^{-1})		
	0	0.10	0.20	0.40	240	280	320	360	12.0	16.0	20.0
E_{corr} (mV)	− 51.3	− 203.2	− 245.8	− 282.4	− 113.4	− 162.8	− 243.5	− 281.6	− 203.2	− 208.8	− 223.4
i_{corr} (μA·cm^{-2})	10.8	39.8	101.3	126.1	128.8	177.8	302.0	371.5	39.8	41.7	44.6

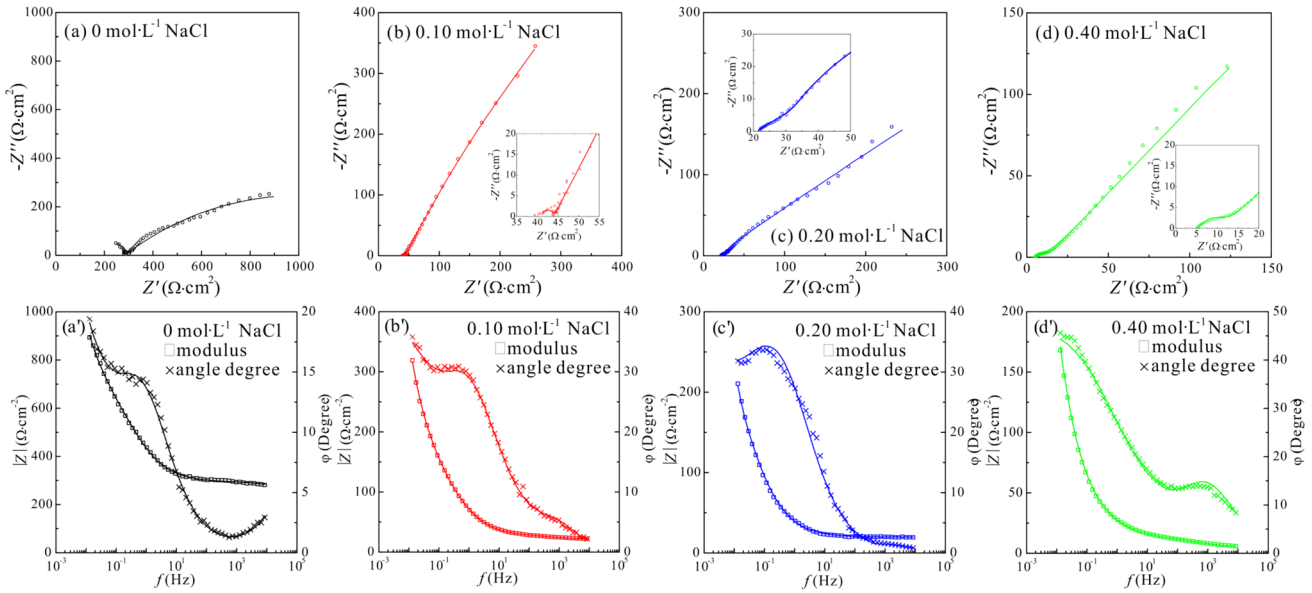

Fig. 3 Nyquist (**a**–**d**) and Bode (**a′**–**d′**) plots of curve of arsenopyrite electrode before and after eroded in different concentrations of sodium chloride at 320 °C and 12.0 MPa, where °,, □ and × represent the experimental values and — represents the simulated values

medium frequencies is associated with the charge transfer resistance (R_t) between the electrode surface and the outer Helmholtz plane of the electrical double layer. The loop at low frequencies is a Warburg diffusion component, which corresponds to the diffusion process of liquid-phase ions. Figure S2 illustrates the electrochemical equivalent circuit (EEC) that stimulated the electrochemical oxidation of arsenopyrite, wherein R_s is the solution ohmic resistance, R_t is the charge transfer resistance, R_f is the passive film resistance, and CPE_{dl} and CPE_f are the constant phase elements for substituting charge transfer capacitance (C_{dl}) at the double layer and passive film capacitance (C_f) at the passivation layer, respectively. W is the Warburg impedance. Macdonald (1985) expressed the impedance of the CPE as Eq. (5):

$$Z_{\mathrm{CPE}} = \frac{1}{\mathrm{Y}_0(j\omega)^n} \tag{5}$$

Here, Z_{CPE} is the impedance of the CPE (Ω·cm^2), ω is the angular frequency of the AC voltage (rad s^{-1}), Y_0 is the magnitude of admittance of the CPE (S·cm^{-2}·s^{-n}), and n is a dimensionless value reflecting the extent of deviation of the interface from an ideal capacitor ($n=1$). The detailed impedance parameters are summarized in Table 3. In the presence of NaCl, the values of both charge transfer resistance R_t and passive film resistance R_f dramatically decreased. In addition, the Warburg diffusion impedance dramatically increased. The results show that the presence of NaCl greatly promoted the electrochemical oxidization of arsenopyrite. As the concentration of NaCl continuously increased, the values of R_t and R_f both slightly decreased, and Warburg diffusion steadily increased, indicating that charge transfer and mass transfer became easier in the double layer and passivation film. These results indicate that higher concentration of NaCl accelerated oxidative arsenopyrite dissolution.

Figures S3 and S4 present the Nyquist and Bode plots of arsenopyrite at different temperatures and different pressures, respectively. All these plots also show three time constants, including two capacitive loops and a diffusion tail, meaning that arsenopyrite had the same electrochemical oxidization mechanism as those in different concentrations of NaCl. The EEC shown in Fig. S2 was used to draw the plots, and the model parameters are listed in Table 3. As the temperature or pressure continuously increased, the value of the charge transfer resistance R_t and the passive film resistance R_f both steadily decreased, while Warburg diffusion steadily increased. These results revealed that higher temperatures or pressures also promote charge transfer and ion diffusion at the double layer and inhibit the formation of the passivation film.

Surface characterization

XPS

The chemical states and corresponding contents of As and S were determined using XPS, and the spectra of the pristine and eroded arsenopyrite in different concentrations of NaCl solution are shown in Fig. 4. Five and six doublet peaks were used to fit the As 3*d* and S 2*p* spectra, respectively. The main peak of each doublet was limited to the

Table 3 Model parameters for equivalent circuit

Number	Experimental conditions			R_s ($\Omega \cdot cm^2$)	CPE_f		R_f ($\Omega \cdot cm^2$)	CPE_{dl}		R_t ($\Omega \cdot cm^2$)	W ($S \cdot cm^{-2} \cdot s^{-1/2}$)	χ^2
	C_{NaCl} ($mol \cdot L^{-1}$)	T (°C)	Pressure (MPa)		$Y_{0,1}$ ($S \cdot cm^{-2} \cdot s^{-n_1}$)	n_1		$Y_{0,3}$ ($S \cdot cm^{-2} \cdot s^{-n_3}$)	n_3			
1	0	320	12.0	21.9	1.48E-3	0.62	432.4	3.74E-7	0.59	295.0	8.76E-3	3.58E-3
2	0.10	320	12.0	13.3	3.45E-4	0.75	52.2	1.27E-2	0.65	97.0	1.62E-2	3.72E-3
3	0.20	320	12.0	16.2	1.55E-3	0.60	25.5	1.77E-3	0.99	74.8	2.91E-2	4.28E-3
4	0.40	320	12.0	5.1	1.15E-3	0.63	13.6	1.73E-3	0.62	68.1	3.24E-2	2.54E-4
5	0.20	240	18.5	8.0	3.78E-4	1	6.7	9.13E-3	0.71	101.9	2.44E-2	5.45E-3
6	0.20	280	18.5	7.9	2.14E-2	1	3.3	1.74E-2	0.70	97.1	8.45E-2	2.28E-3
7	0.20	320	18.5	6.7	3.52E-4	1	1.6	1.98E-2	0.74	82.4	1.33E-1	4.35E-3
8	0.20	360	18.5	7.3	2.86E-2	1	1.4	1.15E-2	0.72	77.0	2.40E-1	6.54E-3
9	0.10	320	12.0	13.3	3.45E-4	0.75	52.2	1.27E-2	0.65	97.0	1.62E-1	3.72E-3
10	0.10	320	16.0	7.4	1.43E-3	1	44.5	3.17E-3	0.72	57.9	1.96E-1	4.37E-3
11	0.10	320	20.0	7.3	4.91E-2	1	41.2	4.86E-3	0.70	45.9	2.05E-1	1.35E-4

side with the lower binding energy. Tables S2 and S3 list the fitting results. In the XPS spectrum of pristine arsenopyrite, the main component of the surface arsenic species was As(− I)–S (41.13 eV), which accounted for 53.33%, and the main components of the sulfur species were S^{2-} (161.47 eV) and $(AsS)^{2-}$ (162.18 eV), which accounted for 27.14% and 48.56%, respectively. In the XPS spectra of eroded arsenopyrite in different concentrations of NaCl, the results showed that with an increase in NaCl concentration, the peak intensity of As(V)–O and the content of high oxidation state arsenic (As(III)–O and As(V)–O) gradually increased. In addition, the intensity of the $(AsS)^{2-}$ peak gradually decreased, while the intensity of the peak of SO_4^{2-} increased from 30.90% to 50.61% as the NaCl concentration was increased from 0 to 0.40 $mol \cdot L^{-1}$. The As 3*d* and S 2*p* XPS spectra both implied that increasing the concentration of NaCl can promote the oxidation of arsenopyrite.

Figures S5 and S6 show the As 3*d* and S 2*p* XPS spectra of arsenopyrite were oxidized at different temperatures and different pressures, respectively. The fitted results (Tables S1 and S2) show that the peak intensities of As(V)–O and SO_4^{2-} in the high oxidation states of arsenic and sulfur gradually increased with increasing temperature or pressure. The XPS results revealed that higher NaCl concentrations, temperatures, and pressures are all conducive to oxidative arsenopyrite dissolution.

SEM and EDS

SEM observations and EDS analysis were adopted to determine the surface morphology and elemental analysis of arsenopyrite oxidation under HTHP conditions.

Figure 5 shows the SEM surface morphology and EDS images of arsenopyrite oxidation in different concentrations of NaCl solution under HTHP conditions. The surface of the pristine arsenopyrite was smooth and flat, with only a few small scratches from sanding. The eroded arsenopyrite showed the accumulation of many corrosion products or corrosion pits on their surfaces. In the absence of NaCl, the surface of the arsenopyrite was covered with many acicular oxides and some sheet oxides, which were connected and stacked tightly, almost covering the surface of the arsenopyrite. In the 0.10 $mol \cdot L^{-1}$ NaCl solution, many acicular oxides also appeared on the surface of the arsenopyrite, but the distribution of these acicular oxides was loose and discontinuous, and the density was poor. Furthermore, corrosion pits and holes developed on the surface, and further EDS measurements revealed that oxides were not distributed in the pits and holes. In the 0.20 $mol \cdot L^{-1}$ NaCl solution, the arsenopyrite surface developed small cracks and pores, and it became rugged. The acicular oxides disappeared, and the number of sheet oxides decreased. In the 0.40 $mol \cdot L^{-1}$ NaCl solution, larger corrosion pits developed, and small cracks

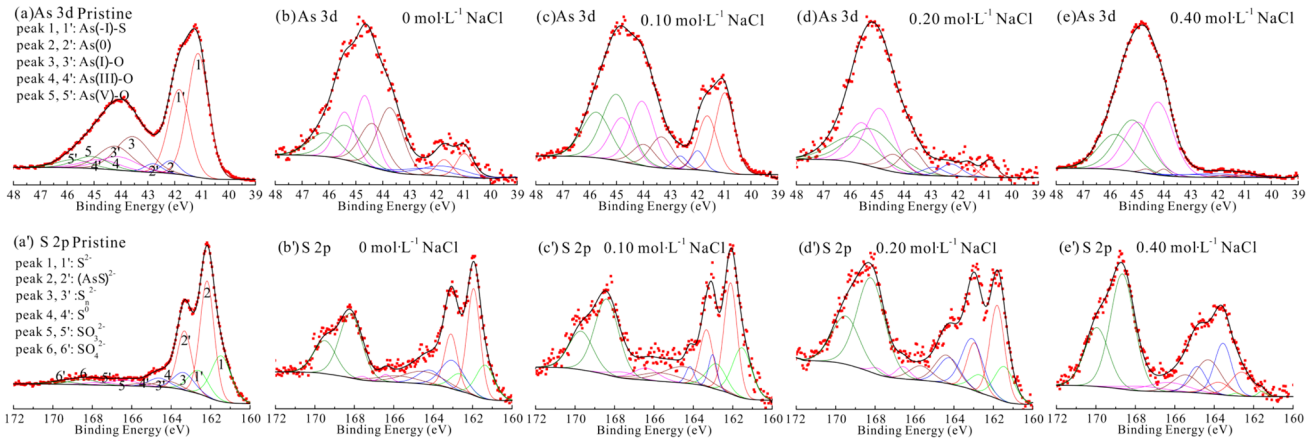

Fig. 4 XPS spectra for As 3*d* (**a**–**e**) and S 2*p* (**a′**–**e′**) of arsenopyrite before and after eroded in different concentrations of NaCl solution (320 °C, 12.0 MPa)

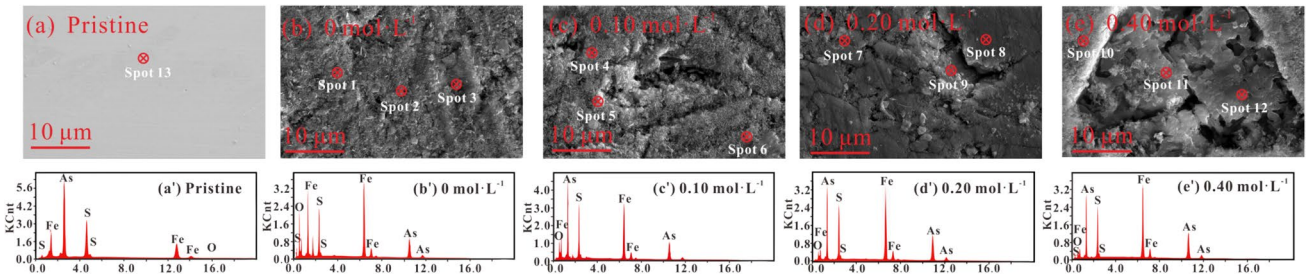

Fig. 5 SEM (**a**–**e**) and EDS (**a′**–**e′**) images of arsenopyrite before and after eroded in different concentrations of NaCl solution (320 °C, 12.0 MPa)

Table 4 The element composition (Atomic %) analysis results of product film of arsenopyrite corrosion under different concentrations of NaCl

Element	0 mol·L^{-1}			0.10 mol·L^{-1}			0.20 mol·L^{-1}			0.40 mol·L^{-1}			Pristine
	Spot 1	Spot 2	Spot 3	Spot 4	Spot 5	Spot 6	Spot 7	Spot 8	Spot 9	Spot 10	Spot 11	Spot 12	Spot 13
O	33.7	39.5	30.4	22.3	28.9	20.4	19.1	12.3	15.6	7.7	8.0	8.2	–
S	17.4	15.8	20.0	24.1	23.2	25.0	26.6	25.5	26.8	24.0	28.0	28.8	35.6
Fe	33.2	27.6	29.5	30.5	27.4	30.9	30.4	25.3	32.1	37.0	35.1	34.6	32.6
As	15.6	17.1	20.1	23.1	20.5	23.7	24.0	36.8	25.4	31.3	28.9	28.4	31.9

and holes appeared in the pits, which confirmed the higher degree of corrosion. The EDS results listed in Table 4 show that pristine arsenopyrite was composed of only S, As and Fe, and the ratio of Fe:As:S (atomic %) was close to 1:1:1. After corrosion, O was observed on the arsenopyrite surface, and the oxygen content of the corroded products tended to decrease with increasing NaCl concentration. As the concentration of Cl^- was increased, the corrosion products on the surface of arsenopyrite were more likely to be destroyed by the chloride ions, releasing oxides into the solution.

Figure S7 shows SEM and EDS images of arsenopyrite oxidation in sodium chloride solution at different temperatures. At 240 and 280 °C, the surface of the corroded arsenopyrite was covered by many acicular oxides and a small amount of sheet material, which was continuous and compact and almost entirely covered the surface of arsenopyrite. When the temperature was increased to 320 °C and 360 °C, the surface of arsenopyrite experienced significant corrosion and developed obvious corrosion pits. Elemental analysis (Table S4) showed that the products contained O, and as the temperature was increased from 240 °C to 360 °C, the percent O tended to decrease, while the contents of S and As tended to increase.

Figure S8 shows the SEM and EDS images of arsenopyrite oxidation at different pressures. When the pressure was increased from 12.0 MPa to 16.0 MPa, many acicular oxides and a small amount of sheet material with obvious corrosion pits appeared on the surface. The elemental composition results listed in Table S5 shows that arsenopyrite was oxidized; however, the elemental composition of the surface products changed little with increasing pressure.

Higher concentrations of NaCl, higher temperatures, and higher pressures all resulted in a significant decrease in the concentration of S and As in the corroded arsenopyrite compared to those in pristine arsenopyrite, suggesting that the above conditions accelerate oxidative arsenopyrite dissolution. In the corroded arsenopyrite, the amount of Fe decreased only slightly, possibly because S and As were converted into soluble ions or ionic components of the solution during corrosion, whereas Fe may have formed an iron oxide (or iron hydroxide) and remained attached to the surface of the arsenopyrite.

Raman spectroscopy

The Raman spectra of pristine and corroded arsenopyrite specimens under different HTHP conditions are shown in Fig. 6. The Raman spectra had identical Raman peaks. In the spectrum of the pristine arsenopyrite specimen, two obvious peaks appeared at 212 and 274 cm^{-1}, which are typical characteristic Raman peaks of arsenopyrite (Mernagh and Trudu 1993). After corrosion under HTHP conditions, 6 new Raman peaks appeared at 389, 470–475, 586, 650, 1065, and 1310 cm^{-1}. The Raman peaks at 389, 586 and 650 cm^{-1} were assigned to α-FeOOH (Bersani et al. 1999; Das and Hendry 2011; Shim and Duffy 2002). The Raman peaks at 650 and 1065 cm^{-1} reflect the characteristics of γ-FeOOH species (Bersani et al. 1999; Das and Hendry 2011; de Faria et al. 1997; Shim and Duffy 2002). The peak at 1310 cm^{-1} resulted from the α-Fe_2O_3 species (Bersani et al. 1999; De Faria et al. 1997; Shim and Duffy 2002), and the peak at 470–475 cm^{-1} was assigned to the polysulfide species (Lara et al. 2016; Mycroft et al. 1990; Parker et al. 2008; Toniazzo et al. 1999). The Raman peak positions of the S, As, and Fe species are summarized in Table 5.

Discussion

Mechanism of the electrochemical oxidation and dissolution of arsenopyrite

Through the results of both the electrochemical measurements and surface analyses, a reasonable oxidative mechanistic route for arsenopyrite was derived, as presented in Fig. 7. The results are corresponding with the results of natural arsenopyrite geochemical evolution in Enguiales, Aveyron, France (Courtin-nomade et al. 2010). At near neutral pH, the formation of elemental sulfur rings from altered arsenopyrite is observed along with the release of Fe and As, which subsequently form more or less crystalline iron arsenate. Other arsenopyrite grains show a complete pseudomorph by elemental sulfur and poorly crystalline iron arsenate [$Fe_3(AsO_4)_2$•xH_2O] distributed around, which may be subsequently transformed to As-rich goethite.

During the electrochemical process, arsenopyrite serves as the anode and is oxidized to Fe^{2+}, AsO_3^{3-}, and S^0 according to reaction (2). Oxygen serves as the oxidizing agent, and the reduction reaction is a cathodic reaction (6):

$$O_2(g) + 2H_2O(l) + 4e^- \rightarrow 4OH^-(aq) \quad (6)$$

The anodic product, AsO_3^{3-}, likely transforms into AsO_4^{3-} via dissolution as shown in reaction (7) (Deng and Gu 2018):

$$AsO_3^{3-}(aq) + H_2O(l) \rightarrow AsO_4^{3-}(aq) + 2H^+(aq) + 2e^- \quad (7)$$

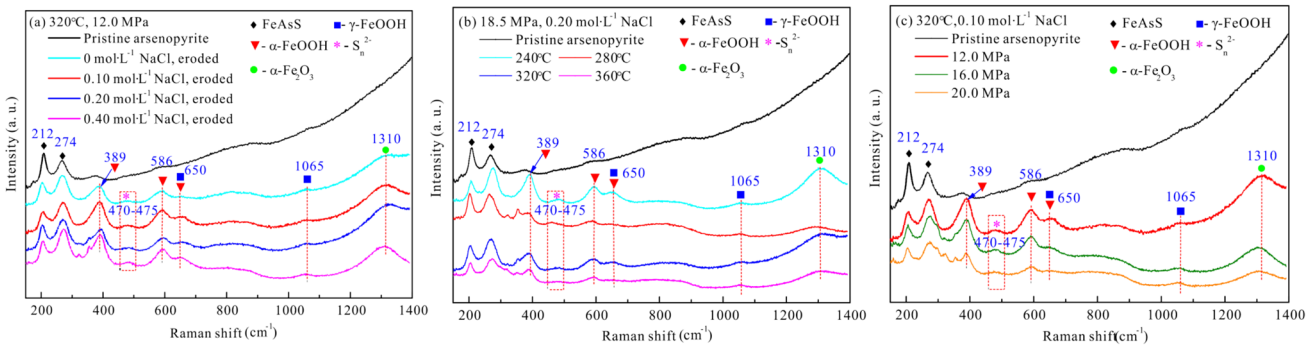

Fig. 6 Raman images of the pristine and eroded arsenopyrite, where **a** different concentrations NaCl solution, **b** different temperatures and **c** different pressures

Table 5 Summary of Raman peak position of sulfur, arsenic, and iron species

Species	Raman shift (cm^{-1})	References
FeAsS	203, 244, 296, 334, 369, 404	Lara et al. (2016); McGuire et al. (2001)
	212, 274, 388, 481, 527, 582	Mernagh and Trudu (1993)
	212, 274	This work
α-FeOOH	301–318, 389, 580–586, 650, 1305–1320	Bersani et al. (1999); Das and Hendry (2011); Shim and Duffy (2002)
	389, 586, 650	This work
γ-FeOOH	217–223, 255–270, 383, 528, 650, 1065–1165	Bersani et al. (1999); Das and Hendry (2011); De Faria et al. (1997); Shim and Duffy (2002)
	650, 1065	This work
α-Fe_2O_3	1310	Bersani et al. (1999); De Faria et al. (1997); Shim and Duffy (2002)
	1310	This work
Polysulfides	418, 443–475	Lara et al. (2016); Mycroft et al. (1990); Parker et al. (2008); Toniazzo et al. (1999)
	470–475	This work

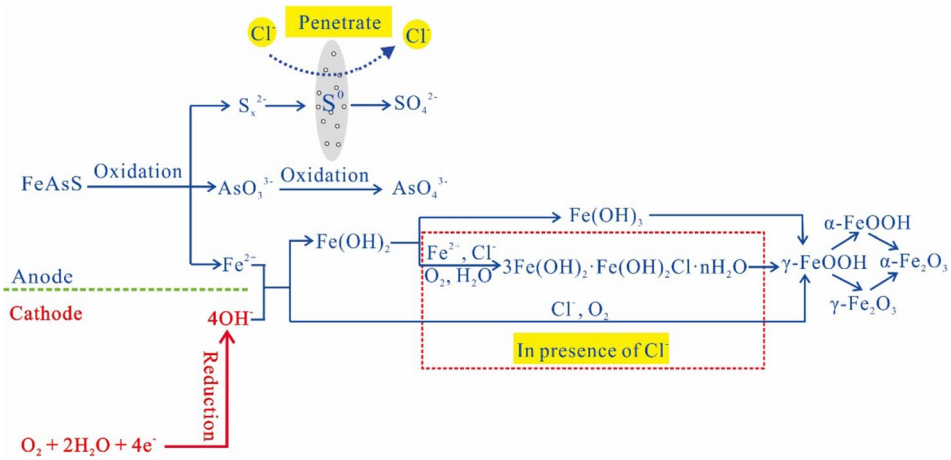

Fig. 7 Electrochemical mechanism of arsenopyrite oxidative dissolution at high temperature and high pressure

The precursor to the anodic product S^0 is believed to be polysulfide S_n^{2-} (Steudel 1996), and the transformation processes can be expressed as reactions (8) to (10). First, FeAsS decomposed to Fe^{2+}, $(AsS)^{2-}$ and S^{2-}, and then S^{2-} underwent dimerization to S_2^{2-} species, which may form on S-terminated surfaces and can be regarded as a further reconstruction of S_n^{2-} (Harmer et al. 2004). S_n^{2-} then transforms into elemental S, which is considered an intermediate and metastable reaction product and, given time, should oxidize into sulfates following reaction (11) (Fernandez et al. 1995; Sanchez and Hiskey 1991; Nesbitt et al. 1995):

$$2S^{2-}(aq) \rightarrow S_2^{2-}(aq) + 2e^- \quad (8)$$

$$nS_2^{2-}(aq) \rightarrow 2S_n^{2-}(aq) + (2n-4)e^- \quad (9)$$

$$S_9^{2-}(aq) + H^+(aq) \leftrightarrow HS_9^-(aq) \leftrightarrow HS^-(aq) + S_8(s) \quad (10)$$

$$2S^0(s) + 4H_2O(l) \rightarrow SO_4^{2-}(aq) + 8H^+(aq) + 8e^- \quad (11)$$

In the absence of Cl^-, the Fe^{2+} ions of the anodic products combine with OH^- and form $Fe(OH)_2$, which is then oxidized into $Fe(OH)_3$ by O_2 and finally transforms into γ-FeOOH following reactions (12) to (14) (Ramya et al. 2018; Zhang et al. 2011):

$$Fe^{2+}(aq) + 2OH^-(aq) \rightarrow Fe(OH)_2(s) \quad (12)$$

$$4Fe(OH)_2(s) + O_2(g) + 2H_2O(l) \rightarrow 4Fe(OH)_3(s) \quad (13)$$

$$Fe(OH)_3(s) \rightarrow \gamma - FeOOH(s) + H_2O(l) \quad (14)$$

In the Raman spectra, α-FeOOH and α-Fe_2O_3 peaks were observed, indicating that some γ-FeOOH transformed into α-FeOOH and α-Fe_2O_3. According to several studies (Kwon

et al. 2007; Majzlan et al. 2007; Nie et al. 2009), this transformation is due to the conversion of FeOOH into Fe_2O_3 through the following processes:

$$8\gamma - \mathrm{FeOOH(s)} \rightarrow 4\gamma - \mathrm{Fe_2O_3(s)} + 4\mathrm{H_2O(l)} \rightarrow 4\alpha - \mathrm{Fe_2O_3(s)} + 4\mathrm{H_2O(l)} \quad (15)$$

$$2\gamma - \mathrm{FeOOH(s)} \rightarrow 2\alpha - \mathrm{FeOOH(s)} \rightarrow \alpha - \mathrm{Fe_2O_3(s)} + \mathrm{H_2O(l)} \quad (16)$$

Notably, the above transformation from γ-Fe_2O_3 to α-Fe_2O_3 is not possible under thermodynamic conditions. FeOOH is more thermodynamically stable than γ-Fe_2O_3, and α-Fe_2O_3 cannot be formed in situ (Zhang et al. 2011). However, when exposed to a dry atmosphere, the formation of α-Fe_2O_3 is feasible through a dehydration reaction, and the reaction proceeds via α-FeOOH or γ-Fe_2O_3 (Zhang et al. 2011, 2009; Nie et al. 2009). The ex situ Raman analysis confirmed the formation of α-Fe_2O_3.

Zhang et al. (2011) confirmed that in the presence of Cl^-, the Fe^{2+} ions of the anodic products would directly oxidize to FeOOH without involving $Fe(OH)_2$ or $Fe(OH)_3$. During this process, Cl^- ions can accelerate arsenopyrite oxidization by promoting anodic dissolution, acting as a catalyst. This result is consistent with the results of the electrochemical tests:

$$4\mathrm{FeCl_2(s)} + 8\mathrm{OH^-(aq)} + \mathrm{O_2(g)} \rightarrow 4\mathrm{FeOOH(s)} + 8\mathrm{Cl^-(aq)} + 2\mathrm{H_2O(l)} \quad (17)$$

In addition, many researchers (Simard 2001; Boucherit and Hugot-Le Goff 1992; Refait and Genin 1993) believe that a thin, unstable, colloidal hydroxyl salt layer called "green rust" forms prior to the transformation of Fe^{2+} into γ-FeOOH. Green rust, $3Fe(OH)_2{\cdot}Fe(OH)_2Cl{\cdot}nH_2O$, forms under the action of oxygen and chloride:

$$7\mathrm{Fe(OH)_2(s)} + \mathrm{Fe^{2+}(aq)} + 2\mathrm{Cl^-(aq)} + 1/2\mathrm{O_2(g)} + (2n+1)\mathrm{H_2O(l)} \rightarrow 2\left[3\mathrm{Fe(OH)_2 \cdot Fe(OH)_2Cl \cdot nH_2O}\right](s) \quad (18)$$

Generally, green rust is not stable and undergoes further transformation to γ-FeOOH (lepidocrocite) via reaction (19) (Ramya et al. 2018; Boucherit et al. 1992; Zhang et al. 2011) and may even transform to γ-Fe_2O_3 and α-Fe_2O_3 via reactions (15) and (16):

$$3\mathrm{Fe(OH)_2 \cdot Fe(OH)_2Cl \cdot nH_2O} \rightarrow \left[\mathrm{Fe(H_2O)_x}\right]\mathrm{Cl_2} \rightarrow \gamma - \mathrm{FeOOH},\ \mathrm{FeOCl} + \mathrm{H_2O} \rightarrow \gamma - \mathrm{FeOOH} \quad (19)$$

Geological significance

Thermodynamic stability of arsenopyrite at HTHP

Arsenopyrite is widely distributed in Nature, and it is susceptible to corrosion by oxygen and aqueous solutions. Temperature and pressure, important external factors that affect oxidation reactions, are bound to have an important influence on the oxidation metamorphism of arsenopyrite in Nature. Limited by experimental means, the thermodynamic stability of arsenopyrite in HTHP environments, such as submarine hydrothermal environments, has rarely been investigated. As mentioned above, the open-circuit potential of arsenopyrite without an external current accurately reflect the thermodynamic stability of the system in which it is located. In other words, the more negative the open-circuit potential is, the lower the stability of arsenopyrite and the greater the oxidation tendency.

Previous studies have shown that the dissolution and precipitation of massive sulfides under HTHP hydrothermal conditions cannot be separated from the action of the NaCl medium system (Wang et al. 2017; Toner et al. 2008). The OCP at different concentrations of NaCl and under HTHP conditions confirmed the following observations: (1) at the same high temperatures and pressures, arsenopyrite is more unstable in an environment with a higher concentration of sodium chloride (salinity); (2) in a system with constant salinity and pressure, arsenopyrite becomes more unstable with increasing temperature; and (3) in a system with constant salinity and temperature, the thermodynamic stability of arsenopyrite decreases with increasing pressure. Furthermore, arsenopyrite transforms into haematite under high temperature and pressure, indicating that haematite is more thermodynamically stable. The results of this study have important significance for modern submarine hydrothermal mineralization.

Oxidative dissolution rate: effect of NaCl concentration, temperature and pressure

During the dissolution of arsenopyrite, Fe and As are released and transformed. The NaCl concentration, temperature, and pressure are important factors affecting the dissolution rate of arsenopyrite.

The oxidative dissolution rate is one of the important dynamic parameters of arsenopyrite oxidation, and it can be calculated using the Faraday equation (Eom 2013) based on the corrosion current density i_{corr}:

$$v = \frac{Mi_{corr}}{nF} \quad (20)$$

Table 6 Summary of the dissolution rates of arsenopyrite in different conditions

No	Solution conditions	Rate constants ($mol \cdot m^{-2} \cdot s^{-1}$)	References
1	15 ~ 45 °C, pH 1.8, 0.01 $mol \cdot L^{-1}$ $Fe_2(SO_4)_3$	10^{-6}	Yu et al. (2004b)
2	25 °C, pH 6.3 ~ 6.7, 0.3 ~ 17 $mg \cdot L^{-1}$ O_2	$10^{-10.14 \pm 0.03}$	Walker et al. (2006)
3	10 ~ 40 °C, pH 2.0, 1.0 $mol \cdot L^{-1}$ Fe^{3+}	10^{-5}	McKibben et al. (2008)
4	10 ~ 40 °C, pH 2.0 ~ 4.5, 1.0 atm O_2	$10^{-6.11}$	McKibben et al. (2008)
5	240 ~ 360 °C, 18.5 MPa, 0.20 $mol \cdot L^{-1}$ NaCl	8.0×10^{-5}	This work

where v is the dissolution rate, $g \cdot m^{-2} \cdot h^{-1}$, i_{corr} is the corrosion current density, $\mu A \cdot cm^{-2}$, M is the atomic weight, g·mol, n is the valence state, and F is the Faraday constant, 96,485 C·mol.

When arsenopyrite was oxidized in a 0.2 $mol \cdot L^{-1}$ NaCl solution (18.5 MPa), at 240 °C, the i_{corr} value was 128.8 $\mu A \cdot cm^{-2}$, corresponding to an activated dissolution rate of 6.675×10^{-6} $mol \cdot m^{-2} \cdot S^{-1}$. This result implies that 1.175×10^4 g Fe(II) would be released per square meter in 1 year. At 280 °C, the i_{corr} value increased to 177.8 $\mu A \cdot cm^{-2}$, and the activated dissolution rate was 9.214×10^{-6} $mol \cdot m^{-2} \cdot S^{-1}$, reflecting an increased release of 1.623×10^4 g Fe(II) per year. When the temperature was continuously increased to 320 and 360 °C, the i_{corr} values were 1.565×10^{-5} and 1.925×10^{-5} $mol \cdot m^{-2} \cdot S^{-1}$, respectively. The relationship between i_{corr} and T is shown in Fig. S9a, which reveals that the i_{corr} of arsenopyrite and $1/T$ have a negative linear relationship between 240 °C and 360 °C; that is, $i_{corr} = -687{,}621/T + 1452.1$, and the coefficient of determination (R^2) is 0.9634. Moreover, this result confirmed that increasing the temperature accelerates arsenopyrite oxidation. The relationships between temperature ($1/T$) and corrosion rate (k) are shown in Fig. S9b. The result shows that they have a linear relationship: $k = -0.0356/T + 8.0 \times 10^{-5}$. Although some studies have reported the dissolution rate constant of arsenopyrite at ambient temperature or no more than 100 °C and ambient pressure, the dissolution rate constant of arsenopyrite under HTHP conditions has not been reported thus far. Through kinetic experiments conducted in a mixed flow reactor, Yu et al. (2004b) studied arsenopyrite oxidation in pH 1.8 $Fe_2(SO_4)_3$ solutions at concentrations of 1×10^{-2} to 1×10^{-5} $mol \cdot kg^{-1}$ and temperatures between 15 and 45 °C. The results confirmed that the rate of arsenopyrite oxidation increased with increasing dissolved $Fe_2(SO_4)_3$ and higher temperatures, with an oxidation rate of 10^{-6} $mol \bullet m^{-2} \bullet s^{-1}$. Walker et al. (2006) used a mixed flow reactor system to study the rate of arsenopyrite oxidation by DO and its mechanism at 25 °C and circumneutral pH. The results revealed that in circumneutral environments (pH 6.3–6.7), the rate of arsenopyrite oxidation was $110^{-10.14 \pm 0.03}$ $mol \bullet m^{-2} \bullet s^{-1}$, and the slow reduction of water at anodic sites on the arsenopyrite surface was the rate-determining step. McKibben et al. (2008) investigated the irreversible inorganic aqueous oxidation of arsenopyrite by dissolved O_2, Fe^{3+}, and NO_3^- at pH 2–4.5 and 10–40 °C with an ionic strength of 0.01 M. The specific rate constants (molal) for arsenopyrite oxidation by dissolved Fe^{3+} (pH 2) and O_2 (pH 2–4.5) were 10^{-5} and $10^{-6.11}$, respectively. The dissolution rates of arsenopyrite under different conditions are summarized in Table 6.

With different NaCl concentrations at 320 °C and 12.0 MPa, the relationship of the corrosion density of arsenopyrite and the concentration of NaCl was $i_{corr} = 297.49 C_{NaCl} + 17.44$, and the coefficient of determination (R^2) was 0.9634 (Fig. S9(c)). This result suggests that a higher concentration of NaCl prompts arsenopyrite dissolution.

With increasing pressure from 12.0 to 20.0 MPa at 0.10 $mol \cdot L^{-1}$ NaCl and 320 °C, the relationship between corrosion density and pressure was $i_{corr} = 0.6P + 32.433$, and the coefficient of determination (R^2) was 0.9857 (Fig. S9(d)). The result reveals that increased pressure is beneficial for the dissolution of arsenopyrite. This result is significant for arsenopyrite pressure leaching in hydrometallurgy.

Conclusions

The electrochemical oxidation behaviors of arsenopyrite in pure water and solutions with different concentrations of NaCl (0–0.40 $mol \cdot L^{-1}$) were studied using in situ electrochemical techniques and surface analysis at temperatures from 240 to 360 °C and pressures from 12.0 to 20.0 MPa.

The OCP of arsenopyrite was found to shift towards negative values with increasing NaCl concentration, temperature, and pressure, suggesting that the thermodynamic stability of arsenopyrite weakens and arsenopyrite becomes more susceptible to oxidation under HTHP conditions. According to the polarization curves, higher NaCl concentrations prompt arsenopyrite dissolution, and the relationship between the corrosion density of arsenopyrite and NaCl concentration can be expressed as $i_{corr} = 297.49 C_{NaCl} + 17.44$. Higher temperatures prompt arsenopyrite oxidation, and the temperature ($1/T$) and corrosion rate (k) have a linear relationship: $k = -0.0356/T + 8.0 \times 10^{-5}$ within the temperature range of 240–360 °C; this result has not been reported in the previous

literature. Higher pressure accelerates the rate of arsenopyrite oxidation, and the relationship between corrosion density and pressure can be expressed as $i_{corr} = 0.6P + 32.433$. The Raman and XPS results showed that arsenopyrite was oxidized to S^0, As(III), and Fe(II) and ultimately transformed to SO_4^{2-}, AsO_4^{3-}, α-FeOOH, γ-FeOOH, and Fe_2O_3 under HTHP conditions.

These findings provide insight into the process of arsenopyrite oxidation under HTHP conditions. They may be used to predict the stability and dissolution of arsenopyrite under HTHP conditions, which would provide deeper insight into the geochemical circulation of Fe, As and S under hydrothermal conditions.

Supplementary Information The online version contains supplementary material available at https://doi.org/10.1007/s00410-022-01929-2.

Acknowledgements This work was financially supported by the National Natural Science Foundation of China (U1812402), the National Natural Science Foundation of China (41873074), and the National Major Scientific Instruments and Equipment's Development Project of National Natural Science Foundation of China (41827802).

Declarations

Conflict of interest The authors declare that they have no known competing financial interests or personal relationships that could have appeared to influence the work reported in this paper.

References

Bard AJ, Faulkner LR (2001) Electrochemical methods: fundamentals and applications, 2nd edn. Wiley and Sons, Hoboken

Bersani D, Lottici PP, Montenero A (1999) Micro-Raman investigation of iron oxide films and powders produced by Sol-Gel Syntheses. J Raman Spectrosc 30:355–360

Boucherit N, Hugot-Le Goff A (1992) Localized corrosion processes in iron and steels studied by in situ Raman spectroscopy. Faraday Discuss 94:137–147

Boucherit N, Hugot-Le Goff A, Joiret S (1992) Influence of Ni, Mo, and Cr on pitting corrosion of steels studied by Raman spectroscopy. Corrosion 48:569–578

Buckley AN, Walker GW (1988) The surface composition of arsenopyrite exposed to oxidising environments. Appl Surf Sci 35:227–240

Courtin-nomade A, Bril H, Beny JM, Kunz M, Tamura N (2010) Sulfide oxidation observed using micro-Raman spectroscopy and micro-X-ray diffraction: the importance of water/rock ratios and pH conditions. Am Miner 95(4):582–591

Das S, Hendry MJ (2011) Application of Raman spectroscopy to identify iron minerals commonly found in mine wastes. Chem Geol 290:101–108

de Faria DLA, Venaüncio Silva S, de Oliveira MT (1997) Raman microspectroscopy of some iron oxides and oxyhydroxides. J Raman Spectrosc 28:873–878

Deng S, Gu GH (2018) An electrochemical impedance spectroscopy study of arsenopyrite oxidation in the presence of Sulfobacillus thermosulfidooxidans. Electrochim Acta 287:106–114

Eom H (2013) Faraday's law of induction. Primary theory of electromagnetics. Power Systems. Springer, Dordrecht

Fernandez MGM, Mustin C, de Donato P, Barres O, Marion P, Berthelin J (1995) Occurrences at mineral–bacterial interface during oxidation of arsenopyrite by Thiobacillus ferrooxidans. Biotechnol Bioeng 46:13–21

Fernandez PG, Linge HG, Wadsley MW (1996a) Oxidation of arsenopyrite (FeAsS) in acid part I: reactivity of arsenopyrite. J Appl Electrochem 26:575–583

Fernandez PG, Lingem HG, Willing MJ (1996b) Oxidation of arsenopyrite (FeAsS) in acid. part II. Stoichiometry and reaction scheme. J Appl Electrochem 26:585–591

Harmer SL, Pratt AR, Nesbitt WH, Fleet ME (2004) Sulfur species at chalcopyrite ($CuFeS_2$) fracture surfaces. Am Mineral 89:1026–1032

Heinrich CA, Seward TM (1990) A spectrophotometric study of aqueous iron(II) chloride complexing from 25 to 200°C. Geochim Cosmochim Acta 54:2207–2221

Kwon SK, Shinoda K, Shigeru S, Waseda Y (2007) Influence of silicon on local structure and morphology of γ–FeOOH and α–FeOOH particles. Corros Sci 49:1513–1526

Lara RH, Ramírez-Aldaba H, Valles OP (2016) Chemical and surface analysis during evolution of arsenopyrite oxidation by Acidithiobacillus thiooxidans in the presence and absence of supplementary arsenic. Sci Total Environ 566–567:1106–1119

Lasia A (2002) Electrochemical impedance spectroscopy and its applications. In: Conway BE, Bockris JO, White RE (eds) Modern aspects of electrochemistry. Modern Aspects of Electrochemistry, vol 32. Springer, Boston, MA

Lazaro I, Cruz R, Gonzalez I, Monroy M (1997) Electrochemical oxidation of arsenopyrite in acidic media. Int J Miner Process 50:63–75

Li Q, Yang YB, Jiang T (2006) Electrochemical oxidation of arsenopyrite in acidic media. Chin J Nonferrous Met 16:1971–1975

Li YQ, He Q, Chen JH (2015) Electronic and chemical structures of pyrite and arsenopyrite. Mineral Mag 79:1779–1789

Lin SY, Liu RQ, Bu YJ, Wang C, Wang L, Sun L, Hu YH (2018) Oxidative depression of arsenopyrite by using calcium hypochlorite and sodium humate. Minerals 8:463–477

Lin S, Li HP, Xu LP, Zhang YQ, Cui C (2017) A novel experimental device for electrochemical measurements in supercritical fluids up to 700°C/1000 bar and its application in the corrosion study of superalloy Inconel 740H. RSC Adv 7:33914–33920

Macdonald DD, Scott AC, Wentrcek P (1979) External reference electrode for use in high temperature aqueous systems. J Electrochem Soc 126:908–911

Macdonald JR (1985) Generalizations of "universal dielectric response" and a general distribution of activation energies model for dielectric and conducting systems. J Appl Phys 58:1971–1978

Majzlan J, Mazeina L, Navrotsky A (2007) Enthalpy of water adsorption and surface enthalpy of lepidocrocite (γ–FeOOH). Geochim Cosmochim Acta 71:615–623

McGuire MM, Jallad KN, Ben-Amotz D, Hamers RJ (2001) Chemical mapping of elemental sulfur on pyrite and arsenopyrite surfaces using near-infrared Raman imaging microscopy. Appl Surf Sci 178:105–115

McKibben MA, Tallant BA, del Angel JK (2008) Kinetics of inorganic arsenopyrite oxidation in acidic aqueous solutions. Appl Geochem 23:121–135

Mernagh TP, Trudu AG (1993) A laser Raman microprobe study of some geologically important sulphide minerals. Chem Geol 103:113–127

Mikhlin YL, Romanchenko AS, Asanov IP (2006) Oxidation of arsenopyrite and deposition of gold on the oxidized surfaces: A scanning

probe microscopy, tunneling spectroscopy and XPS study. Geochim Cosmochim Acta 70:4874–4888
Mikhlin Y, Tomashevich Y (2005) Pristine and reacted surfaces of pyrrhotite and arsenopyrite as studied by X–ray absorption near–edge structure spectroscopy. Phys Chem Miner 32:19–27
Mycroft JR, Bancroft GM, McIntyre NS, Lorimer JW, Hill IR (1990) Detection of sulphur and polysulphides on electrochemically oxidized pyrite surfaces by X–ray photoelectron spectroscopy and Raman spectroscopy. J Electroanal Chem 292:139–152
Neil C, Jun Y (2016) Promotion of arsenopyrite dissolution and secondary mineral formation and phase transformation by aqueous Fe^{3+}. Abstracts of Papers–am Chem Soc 251:63
Neil CW, Yang YJ, Schupp D, Ju Y (2014) Water chemistry impacts on arsenic mobilization from arsenopyrite dissolution and secondary mineral precipitation: implications for managed aquifer recharge. Environ Sci Technol 48:4395–4405
Nesbitt HW, Muir IJ (1998) Oxidation states and speciation of secondary products on pyrite and arsenopyrite reacted with mine waste waters and air. Mineral Petrol 62:123–144
Nesbitt HW, Muir IJ, Pratt AR (1995) Oxidation of arsenopyrite by air and airsaturated, distilled water and implications for mechanisms of oxidation. Geochim Cosmochim Acta 59:1773–1786
Nicol MJ, Guresin N (2003) Anodic behaviour of arsenopyrite and cathodic reduction of ferrate (VI) and oxygen in alkaline solutions. J Appl Electrochem 33:1017–1024
Nie X, Li X, Du C, Huang Y, Du H (2009) Characterization of corrosion products formed on the surface of carbon steel by Raman spectroscopy. J Raman Spec 40:76–79
Osseo–Assare K, Xue T, Ciminelli VST (1984) Solution chemistry of cyanide leaching systems. Precious Metals, Mining Extraction and Processing. AIME, Warrendale, pp 173–197
Papangelakis VG, Demopoulous GP (1990a) Acid pressure oxidation of arsenopyrite. Part I. Reaction Chemistry Can Metall Quart 29:1–12
Papangelakis VG, Demopoulous GP (1990b) Acid pressure oxidation of arsenopyrite. Part II. Reaction Kinetics Can Metall Quart 29:13–20
Parker GK, Woods R, Hope GA (2008) Raman investigation of chalcopyrite oxidation. Coll Surf a: Physicochem Eng Aspects 318:160–168
Parthasarathy H, Liu H, Dzombak DA, Karamalidis AK (2016) The effect of Na–Ca–Cl brines on the dissolution of arsenic from arsenopyrite under geologic carbon dioxide storage conditions. Chem Geol 428:1–7
Pearce CI, Pattrick RAD, Vaughan DJ (2006) Electrical and magnetic properties of sulfides. Rev Mineral Geochem 61:127–180
Pokrovski GS, Kara S, Roux J (2002) Stability and solubility of arsenopyrite, FeAsS, in crustal fluids. Geochim Cosmochim Acta 66:2361–2378
Ramya S, Krishna DNG, Mudali UK (2018) In–situ Raman and X–ray photoelectron spectroscopic studies on the pitting corrosion of modified 9Cr–1Mo steel in neutral chloride solution. Appl Surf Sci 428:1106–1118
Refait P, Genin JMR (1993) The oxidation of ferrous hydroxide in chloride–containing aqueous media and Pourbaix diagrams of green rust one. Corros Sci 34:797–819
Richardson S, Vaughan DJ (1989) Arsenopyrite: a spectroscopic investigation of altered surfaces. Mineral Mag 53:223–229
Sanchez VM, Hiskey JB (1991) Electrochemical behaviour of arsenopyrite in alkaline media. Min Metall Proc 8:1–6
Sanchez VM, Hiskey JB (1998) An electrochemical study of the surface oxidation of arsenopyrite in alkaline media. Metall Mater Trans 19B:943–949
Shim SH, Duffy TS (2002) Raman spectroscopy of Fe_2O_3 to 62 GPa. Am Mineral 87:318–326
Simard S, Odziemkowski M, Irish DE, Brossard L, Ménard H (2001) In situ micro–Raman spectroscopy to investigate pitting corrosion product of 1024 mild steel in phosphate and bicarbonate solutions containing chloride and sulphate ions. J Appl Electrochem 31:913–920
Stefánsson A, Lemke KH, Seward TM (2019) Iron(III) chloride complexation in hydrothermal solutions: a combined spectrophotometric and density functional theory study. Chem Geol 524:77–87
Steudel R (1996) Mechanism for the formation of elemental sulfur from aqueous sulfide in chemical and microbiological desulfurization processes. Ind Eng Chem Res 35:1417–1423
Toner BM, Rouxel O, Santelli CM, Edwards KJ (2008) Sea–floor weathering of hydrothermal chimney sulfides at the East Pacific Rise 9 degrees N: chemical speciation and isotopic signature of Iron using X–ray absorption spectroscopy and laser–ablation MC–ICP–MS. Gastroenterol Jpn 4:234–235
Toniazzo V, Lazaro I, Humbert B (1999) Bioleaching of pyrite by Thiobacillus ferrooxidans: fixed grains electrode to study superficial oxidized compounds. Earth Planet Sci Lett 328:535–540
Tyukova EE, Voroshin SV (2004) Stability of arsenopyrite at temperatures below 300°C. Dokl Earth Sci 399:1240–1244
Walker FP, Schreiber ME, Rimstidt JD (2006) Kinetics of arsenopyrite oxidative dissolution by oxygen. Geochim Cosmochim Acta 70:1668–1676
Wang SF, Jiao BB, Zhang MM, Guo QJ, Wang X, Jia YF (2018) Arsenic release and speciation during the oxidative dissolution of arsenopyrite by O_2 in the absence and presence of EDTA. J Hazard Mater 346:184–190
Wang Y, Han X, Petersen S, Frische M, Qiu Z, Li H, Wu Z, Cui R (2017) Mineralogy and trace element geochemistry of sulfide minerals from the Wocan Hydrothermal Field on the slow–spreading Carlsberg Ridge, Indian Ocean. Ore Geol Rev 84:1–19
Yu YM, Zhu YX, Gao ZM (2004a) Stability of arsenopyrite and As(III) in low–temperature acidic solutions. Sci China Ser D 47:427–436
Yu Y, Zhu Y, Gao Z, Gammons CH, Li D (2007) Rates of arsenopyrite oxidation by oxygen and Fe(III) at pH 1.8–12.6 and 15–45°C. Environ Sci Technol 41:6460–6464
Yu Y, Zhu Y, Williams-Jones AE, Gao Z, Di D (2004b) A kinetic study of the oxidation of arsenopyrite in acidic solutions: implications for the environment. Appl Geochem 19:435–444
Zhang H, Li X, Du C, Qi H, Huang Y (2009) Raman and IR spectroscopy study of corrosion products on the surface of the hot–dip galvanized steel with alkaline mud adhesion. J Raman Spec 40:656–660
Zhang X, Xiao K, Dong CF, Wu JS, Li XG, Huan YZ (2011) In situ Raman spectroscopy study of corrosion products on the surface of carbon steel in solution containing Cl^- and SO_4^{2-}. Eng Fail Anal 18:1981–1989
Zheng K, Li HP, Wang S, Feng XN, Wang LY, Liu QY (2020a) Arsenopyrite weathering in sodium chloride solution: Arsenic geochemical evolution and environmental effects. J Hazard Mater 392:122502
Zheng K, Li HP, Wang S, Wang LY, Liu QY (2020b) Block and malleable arsenopyrite hot–pressure sintering: applied implications. J Mater Res Technol 9:8997–9003